NANO LETTERS

Moiré Skyrmions and Chiral Magnetic Phases in Twisted CrX$_3$ (X = I, Br, and Cl) Bilayers

Muhammad Akram,[†] Harrison LaBollita,[†] Dibyendu Dey, Jesse Kapeghian, Onur Erten,* and Antia S. Botana*

Cite This: *Nano Lett.* 2021, 21, 6633–6639

Read Online

ACCESS | 📊 Metrics & More | 📰 Article Recommendations | 🆂🅸 Supporting Information

ABSTRACT: We present a comprehensive theory of the magnetic phases in twisted bilayer chromium trihalides through a combination of first-principles calculations and atomistic simulations. We show that the stacking-dependent interlayer exchange leads to an effective moiré field that is mostly ferromagnetic with antiferromagnetic patches. A wide range of noncollinear magnetic phases can be stabilized as a function of the twist angle and Dzyaloshinskii–Moriya interaction as a result of the competing interlayer antiferromagnetic coupling and the energy cost for forming domain walls. In particular, we demonstrate that for small twist angles various skyrmion crystal phases can be stabilized in both CrI$_3$ and CrBr$_3$. Our results provide an interpretation for the recent observation of noncollinear magnetic phases in twisted bilayer CrI$_3$ and demonstrate the possibility of engineering further nontrivial magnetic ground states in twisted bilayer chromium trihalides.

KEYWORDS: *2D vdW magnets, CrX$_3$ (X = I, Br, and Cl), moiré patterns, skyrmions*
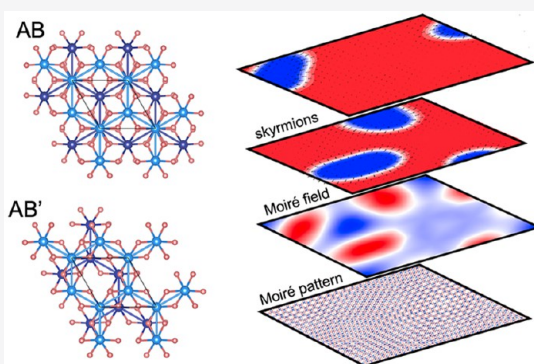
Moiré superlattices arising from twisted bilayers of van der Waals (vdW) crystals represent an ideal platform for studying a plethora of novel phenomena: from the discovery of unconventional superconductivity in twisted bilayer graphene[1] to the recent prediction of noncollinear magnetic states in two-dimensional (2D) magnetic materials.[2−5] Among the currently known 2D vdW magnets, chromium trihalides (CrX$_3$, X = I, Br, and Cl) represent a particularly interesting example in this context. These layered materials consist of ferromagnetic planes of Cr^{3+}: d^3 cations arranged in a honeycomb lattice with edge-sharing octahedral coordination.[6−9] Bulk CrX$_3$ materials exist in two structural phases with different stacking sequences along the c axis: a low-temperature rhombohedral structure and a high-temperature monoclinic structure.[8,10] Recently, it has been shown that the stacking pattern in CrX$_3$ bilayers can give rise to a sign change in the interlayer magnetic coupling.[11−14] This stacking-dependent interlayer magnetic exchange has been experimentally demonstrated in both CrI$_3$ and CrBr$_3$, with the monoclinic stacking supporting an antiferromagnetic (AFM) interlayer coupling, while the rhombohedral stacking supports a ferromagnetic (FM) coupling instead.[15−18] This result has important implications for the moiré physics: a small twisting in bilayers creates a long-period moiré pattern, in which the stacking order in each local region is similar to the corresponding lattice-matched stacking configuration. As such, the competing stacking-dependent interlayer interactions

can give rise to novel magnetic states upon twisting, as recently demonstrated for CrI$_3$.[19]

In this Letter, we study the magnetic phases in twisted bilayer CrX$_3$ spanning all three halide ions using a combination of *ab initio* calculations and atomistic simulations. We show that the interlayer exchange is mostly FM with three symmetry-related AFM patches. Noncollinear magnetic states, including skyrmion crystals, are obtained at small twist angles. These nontrivial phases arise from the competition between the interlayer AFM coupling in the monoclinic stacking regions of the moiré superlattice and the energy cost to form AFM–FM domain walls. Our results agree with recent magnetic circular dichroism (MCD) experiments in CrI$_3$[19] and provide insights for the wealth of noncollinear magnetic phases that can potentially be obtained in twisted bilayer chromium trihalides.
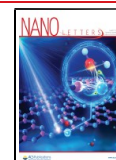
We start by presenting the spin Hamiltonian that will enable the description of the magnetic properties of CrX$_3$ bilayers upon twisting

$$\mathcal{H} = \mathcal{H}^1_{\text{intra}} + \mathcal{H}^2_{\text{intra}} + \mathcal{H}_{\text{inter}} \tag{1}$$
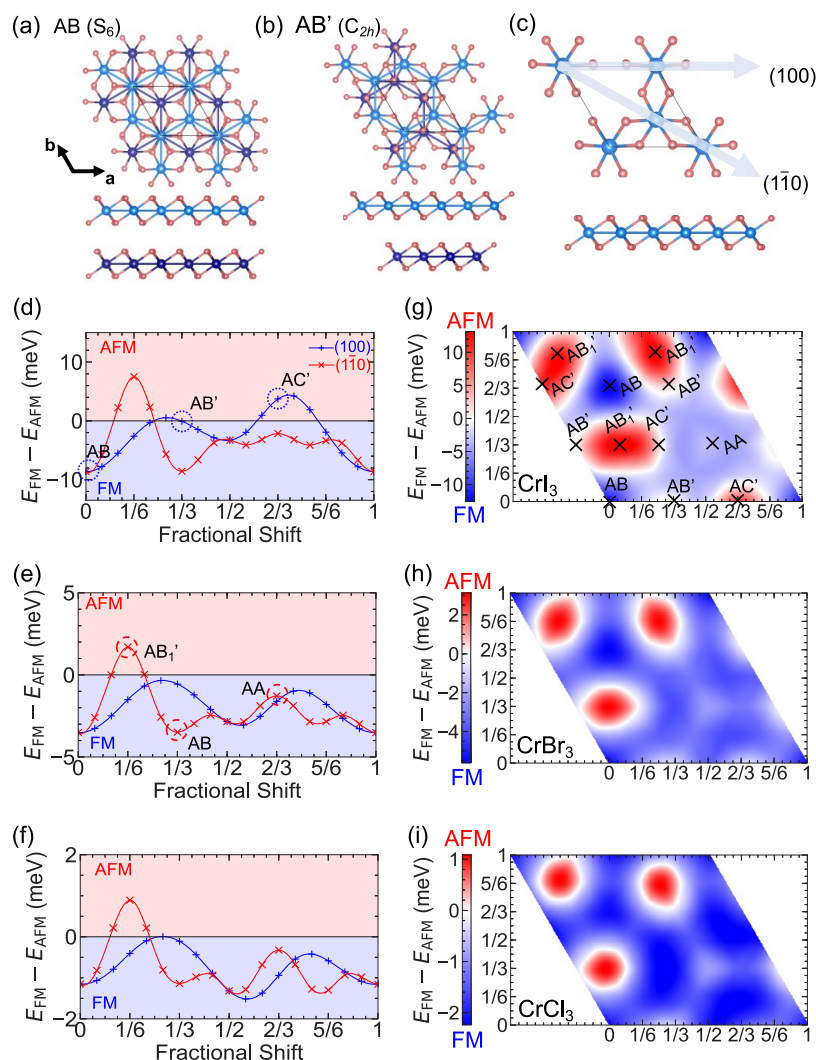
Figure 1. Top and side views of CrX$_3$ bilayers are shown in panels a and b for rhombohedral (AB) and monoclinic (AB′) stacking, respectively. The unit cells are outlined in both cases. The larger, light (dark) blue spheres represent the Cr atoms in the top (bottom) layer, while the smaller, red spheres represent the halide anions. (c) CrX$_3$ monolayer unit cell (top and side view), where the high-symmetry lateral shift directions [100] and [1$\bar{1}$0] are indicated by arrows. (d−f) Energy difference ($E_{FM} - E_{AFM}$) for various stacking displacements along the high-symmetry directions (100) (blue) and (1$\bar{1}$0) (red) for CrI$_3$, CrBr$_3$, and CrCl$_3$ bilayers, respectively. A positive energy difference denotes an AFM ground state, while a negative difference denotes a FM ground state. (g−i) Moiré field patterns calculated for CrI$_3$, CrBr$_3$, and CrCl$_3$ bilayers, respectively. The patterns are obtained by interpolating the data in panels d−f via fitting to a polynomial. Blue regions correspond to a FM interlayer coupling, while red regions correspond to an AFM interlayer coupling. Specific stacking sequences defined in the main text are labeled in panel g, and the corresponding lateral shifts are denoted in panels d and e. The Supporting Information offers further details.

where $\mathcal{H}_{intra}^{1(2)}$ includes the symmetry-allowed intraplane exchange terms in layer 1 (2) and $\mathcal{H}_{inter}$ incorporates the interlayer exchange

$$\mathcal{H}_{intra} = -\frac{J}{2}\sum_{i,\mu}\mathbf{S}_i\cdot\mathbf{S}_{i+\hat{\delta}_\mu} - \frac{\lambda}{2}\sum_{i,\mu}S_i^z S_{i+\hat{\delta}_\mu}^z$$

$$-\frac{D}{2}\sum_{i,\mu}[\hat{d}_\mu\cdot(\mathbf{S}_i\times\mathbf{S}_{i+\hat{\delta}_\mu})] - A_s\sum_i (S_i^z)^2 \quad (2)$$

$$\mathcal{H}_{inter} = -\sum_{\langle ij\rangle}J^\perp(\mathbf{r}_{ij})\mathbf{S}_i^1\cdot\mathbf{S}_j^2 \quad (3)$$

Here, i is the site index, and $\hat{\delta}_\mu$ are the three nearest neighbors (nn) on the honeycomb lattice. J is the intralayer Heisenberg exchange coupling; λ is the anisotropic exchange coupling; and A_s is the single-ion anisotropy. $J^\perp(\mathbf{r}_{ij})$ represents the interlayer

exchange coupling, and $\mathbf{r}_{ij}$ is the interlayer displacement. Estimates for all of these constants are obtained from first-principles calculations (see below). D is the Dzyaloshinskii−Moriya interaction (DMI) and is introduced in the atomistic simulations.

The derivation of $J^\perp$ entails building the CrX$_3$ bilayers. Each bilayer is initially constructed using the rhombohedral stacking with a vacuum of 20 Å along the c axis. The bilayers are subsequently relaxed within a FM state via density functional theory (DFT), as implemented in the Vienna *Ab initio* Simulation Package (VASP)[20] using projector augmented wave pseudopotentials.[21] Different exchange−correlation functionals were attempted with both PBEsol[22] and the DFT-D3 scheme[23] (the latter including vdW interactions), giving an in-plane lattice parameter and interlayer distance that differ from experimental data by less than 1%. On the basis of this

agreement, we proceed using the PBEsol functional throughout (see the Supporting Information for further details).

For small twist angles, the stacking order at any local region in the moiré pattern can be obtained by translating one of the monolayer units in the rhombohedral reference cell by the vector $\mathbf{r} = \eta\mathbf{a} + \nu\mathbf{b}$, where $\eta, \nu \in [0, 1]$ and $\mathbf{a}$ and $\mathbf{b}$ are the lattice vectors of the unit cell. We organize bilayer stacking sequences into two groups: symmetric stacking sequences (rhombohedral) denoted as AB, AA, and BA and asymmetric stacking sequences (monoclinic) denoted as AB′, AB$_1$′, and AC′. All six of these stacking arrangements can be achieved from lateral shifts along two high-symmetry directions: (100) and (1$\bar{1}$0) (panels a−c of Figure 1).

The moiré field is extracted from the stacking-dependent interlayer interaction in these bilayers.[11,13,14] $J^\perp(\mathbf{r})$ in eq 3 for a given stacking is obtained as $(E_{\text{AFM}} - E_{\text{FM}})/2|\mathbf{S}|^2$, with $|\mathbf{S}| = ^3/_2$. Here, E_{FM} and E_{AFM} refer to the DFT energies in a FM state and an A-type AFM state. For the magnetic calculations at different stackings, we have employed DFT+U[24] to treat the localized Cr 3d electrons with an on-site Coulomb repulsion U = 3 eV, consistent with previous literature,[11,12,25] and with constrained random phase approximation (cRPA) calculations on CrI$_3$[26] (see the Supporting Information for further details on the DFT+U calculations). The results for $E_{\text{FM}} - E_{\text{AFM}}$ at different stackings for CrX$_3$ bilayers are shown in panels d−i of Figure 1. As expected, the interlayer exchange modulates from FM to AFM as the stacking is changed; a dominant interlayer FM coupling is obtained with three symmetry-related AFM patches. For all halides, the rotationally symmetric AB, AA, and BA stacking sequences strongly favor a FM interlayer coupling. However, the broken symmetry stackings (AB′, AB$_1$′, and AC′) differ between the three compounds. In CrI$_3$, an AFM coupling in all three stacking sequences is favored, while in CrBr$_3$ and CrCl$_3$, an AFM coupling is preferred only in the AB$_1$′ stacking sequence. Accordingly, a systematic reduction in the size of the AFM regions can be observed in panels g−i of Figure 1 as the size of the halide decreases. These findings agree with recent experimental[18,27] and theoretical work.[11,13,14,28] The sign change in the interlayer exchange can be understood from the competition between AFM nn t_{2g}−t_{2g} couplings and FM next-nn t_{2g}−e_g couplings. In the symmetric stacking sequences, the number of next-nn is greater than the number of nn, leading to an overall FM exchange, while for the asymmetric stacking sequences, the situation is reversed, leading to an AFM exchange.[11,29] First-principles-derived magnetic parameters in vdW magnets differ highly in the literature as a result of the use of different functionals and computational parameters.[29] We have employed a consistent methodology throughout to extract all couplings needed for the atomistic simulations (see the Supporting Information for more details).

To derive J, λ, and A_s from first principles, we follow a procedure analogous to that employed in ref 30 for monolayer CrI$_3$. Specifically, we consider four magnetic configurations in CrX$_3$ monolayers: FM and AFM both oriented in plane (x) and out of plane (z). These calculations are performed using the same methodology described above for the bilayers within PBEsol+U (U = 3 eV), including spin−orbit coupling (SOC) (see the Supporting Information for the energy mappings). The derived values of J, λ, and A_s are shown in Table 1. Importantly, we obtain $J > 0$ (favoring FM interactions) in all materials with a value that decreases from I to Cl, as expected. The derived $A_s > 0$ favors an off-plane easy axis. For CrCl$_3$, this

Table 1. Magnetic Parameters Extracted from DFT Calculations in Monolayer CrX$_3$[a]

	CrI$_3$	CrBr$_3$	CrCl$_3$
J (meV)	4.06	3.42	2.37
λ (meV)	0.14	0.04	0.003
A_s (meV)	0.03	0.03	0.006

^{a}J is the intralayer symmetric Heisenberg exchange coupling; λ is the anisotropic exchange coupling; and A_s is the single ion anisotropy.

result disagrees with experiments;[10] therefore, dipole−dipole interactions have to be included to turn its anisotropy in plane (see the Supporting Information for further details).

We now employ the magnetic parameters derived above and further introduce the DMI for the atomistic simulations. We introduce the DMI in this manner because its first-principles derivation would entail noncollinear calculations beyond the monolayer (where DMI is not allowed by symmetry). Also, this allows us to easily probe changes upon tuning the DMI, something that could be attainable experimentally using different substrates or via liquid ion gating.[31] As such, we consider three different values of the DMI for each material: D/J = 0.05, 0.1, and 0.2. To find the ground state for the bilayer Hamiltonian (eq 1), we take the continuum limit and solve the Landau−Lifshitz−Gilbert (LLG) equation[32]

$$\frac{d\mathbf{m}}{dt} = -\gamma\mathbf{m} \times \mathbf{B}^{\text{eff}} + \alpha\mathbf{m} \times \frac{d\mathbf{m}}{dt} \qquad (4)$$

where $\mathbf{m}$ is the magnetization, $\mathbf{B}^{\text{eff}} = -\delta\mathcal{H}/\delta\mathbf{m}$, γ is the gyromagnetic ratio, and α is the Gilbert damping coefficient. We solve the LLG equations for each layer self-consistently keeping $|\mathbf{m}| = 1$ and imposing periodic boundary conditions. Our method is suitable to capture magnetic phases that are commensurate with the moiré superlattice[4] (see the Supporting Information for further details).

The main results for the magnetic phase diagrams at $T = 0$ are summarized in Figures 2, 4, and 5 for CrI$_3$, CrBr$_3$, and CrCl$_3$, respectively. A plethora of noncollinear phases, including skyrmion crystals (SkX), are obtained at small angles (or large moiré periods) driven by the competing magnetic interactions in the moiré superlattices. Reference 14 has also studied the magnetic phase diagrams of twisted trihalide bilayers, but the DMI was not considered, impeding the stabilization of SkX phases.

We start our discussion of the atomistic simulations with CrI$_3$ bilayers that display the richest phase diagram as a function of the twist angle (panels a−c of Figure 2). For the smallest angles, a 1SkX/2SkX phase is the ground state (Figure 2d). This phase is stabilized when the moiré superlattice is large enough, so that one skyrmion forms in an AFM region on one layer, while two skyrmions form in the remaining two AFM patches on the other layer. For $\theta > 0.72°$, a 1SkX/FM phase is obtained with a single skyrmion forming in the three overlapping AFM regions on one layer, while the other stays FM (Figure 2e). For even larger angles, a noncollinear 1 SkX/spiral (Sp) phase is formed with a single skyrmion in one of the AFM patches on one layer and a spiral in the remaining two AFM regions on the other layer (Figure 2f). As the angle is increased further, a FM + tilted phase is obtained, in which the magnetization is out-of-plane in the FM background but acquires a finite in-plane component in the AFM regions (Figure 2g). The in-plane magnetization is opposite in the two layers, and its magnitude decreases with an increasing angle.
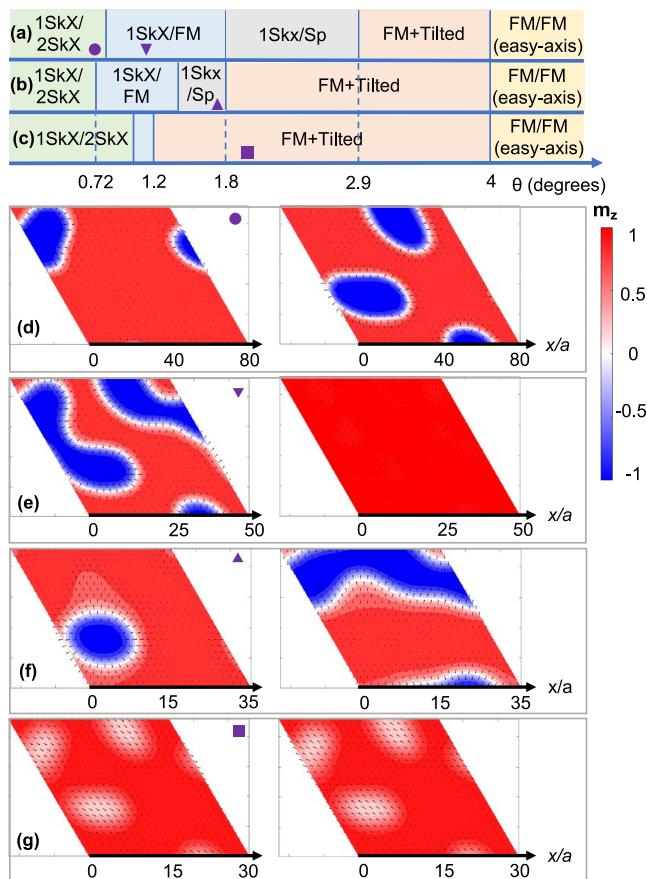
Figure 2. Phase diagram and magnetization textures of twisted bilayer CrI$_3$. (a−c) Phase diagram of twisted bilayer CrI$_3$ as a function of twist angle θ for different values of DMI. Here, panels a, b, and c correspond to D/J = 0.2, 0.1, and 0.05, respectively. (d) Magnetization texture of 1SkX/2SkX for D/J = 0.2 and θ = 0.72°. The 1SkX/2SkX phase competes in energy with a 3SkX/FM state, in which three skyrmions are formed on one layer, while the other remains FM. The 1SkX/2SkX phase has slightly lower energy than the 3SkX/FM phase because it minimizes the skyrmion−skyrmion interactions. However, this energy difference decreases for smaller θ as the distance between the skyrmions becomes larger. (e) Magnetization texture of 1SkX/FM for D/J = 0.2 and θ = 1.15°. (f) Magnetization texture of 1SkX/Sp for D/J = 0.1 and θ = 1.64°. (g) Magnetization texture of FM + tilted state for D/J = 0.05 and θ = 1.91°. The x axis in panels d−g shows the real space position within the moiré unit cell of size $L = a/2 \sin(\theta/2)$, where a is the lattice spacing.

Finally, a transition from the FM + tilted phase to a FM/FM state is obtained at $\theta \sim 4°$. This FM/FM phase is the ground state at large angles for all DMI strengths.

An analytical estimate for the critical twist angle to obtain a skyrmionic phase transition (θ_c) can be derived considering the competition between domain wall energy formation and interlayer exchange energy. Considering a single AFM patch, flipping the magnetization in one of the layers would lower the interlayer exchange energy, producing an energy gain $E_{AFM} \sim 2f_{AFM} \left(\frac{L}{a}\right)^2 \overline{J}^\perp$ (where f_{AFM} is the area fraction of the AFM patch over the moiré unit cell, $\overline{J}^\perp$ is the average AFM coupling, and a is the lattice spacing). This energy scales with the area of the AFM patch and, therefore, varies quadratically with the moiré period, L. On the other hand, this creates a domain wall with the rest of the system of length $\delta \sim \pi((J + \frac{\lambda}{2})/(A_s + \lambda + 0.72\overline{J}^\perp))^{1/2} a$ and energy cost $E_{DW} \sim \left(\frac{\pi}{a}\sqrt{(J + \frac{\lambda}{2})(A_s + \lambda + 0.72\overline{J}^\perp)} - \frac{D\pi}{a}\right)L$. Similar expressions are obtained in ref 19, but we also consider the contribution from the DMI (see the Supporting Information for more details). Importantly, for large enough L, E_{AFM} can overcome E_{DW} and lead to a phase transition to a skyrmionic phase. The critical angle for the transition is determined by minimizing the energy.

$$\theta_c \sim \frac{2f_{AF}\overline{J}^\perp}{\pi\left(\sqrt{\left(J + \frac{\lambda}{2}\right)(A_s + \lambda + 0.72\overline{J}^\perp)} - D\right)} \tag{5}$$

This estimate is for a single domain and, therefore, only applicable when the AFM patches are well-separated. When the domain wall length δ is comparable to the separation between AFM patches (as in CrI$_3$; Figure 1g), there can be more complicated states. In any case, the analytical estimate in CrI$_3$ [$\theta_c \sim 3°$ (D/J = 0.2) and 2.3° (D/J = 0.1)] is in good agreement with our numerical results for the 1SkX/Sp to FM + tilted phase boundary [$\theta_c \sim 2.9°$ (D/J = 0.2) and 1.8° (D/J = 0.1)]. The trends are the expected ones as an increasing DMI decreases the domain wall energy and, therefore, increases θ_c.

Our phase diagram is in agreement with recent experiments on CrI$_3$ bilayers on hexagonal boron nitride (h-BN) substrates that demonstrated their high degree of magnetic tunability upon twisting, gating, and applied magnetic field using MCD.[19] A FM/FM phase is indeed the ground state in these experiments for $\theta > 3°$, while a noncollinear magnetic ground state arises at smaller angles, in agreement with our results. Because these MCD experiments are only sensitive to the z component of the magnetization, further work will be necessary to pinpoint the nature of this noncollinear magnetic phase and to check for the skyrmion phases that we predict.
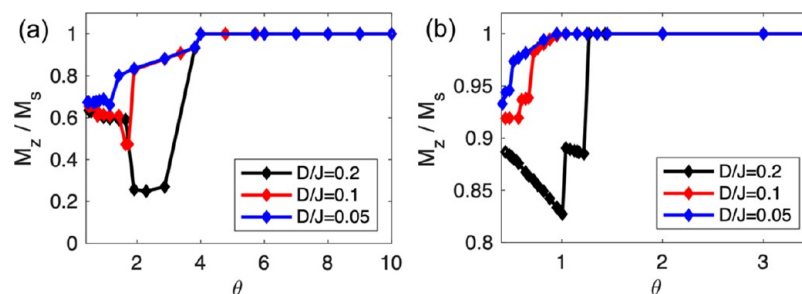

Figure 3. z component of the normalized average magnetization as a function of the twist angle (θ) for (a) CrI$_3$ and (b) CrBr$_3$ for varying D/J.

To make further connections with ref 19, we have also calculated the ratio of the z component of the normalized magnetization (M_z) and the saturation magnetization (M_s) for bilayer CrI_3 (Figure 3a). Experiments show that below $\theta \sim 3°$ M_z/M_s drops gradually to a saturation value of ~ 0.6.[19] Our simulations show a transition of the same nature taking place for $\theta \sim 4°$ with M_z slowly decreasing into the FM + tilted phase as the angle is lowered. For our lowest and intermediate DMIs ($D/J = 0.05$ and 0.1), the magnetization decreases gradually into the different skyrmion phases, until it saturates at small angles to $M_z/M_s \sim 0.65$, close to the experimental value. For the largest DMI ($D/J = 0.2$), the magnetization drops abruptly in the 1SkX/Sp phase instead, recovering the $M_z/M_s \sim 0.65$ value at low angles. This abrupt drop has not been observed in experiments,[19] suggesting that the DMI is smaller in bilayer CrI_3 on h-BN substrates.

Next, we discuss the phase diagram of $CrBr_3$. The ground states are similar to those in CrI_3, with FM/FM and 1SkX/2SkX phases emerging at large and small angles, respectively (panels a−d of Figure 4). At intermediate angles, 2SkX/FM (Figure 4e) and FM + tilted (Figure 4f) states are stabilized. The 2SkX/FM phase has two skyrmions on one layer along with a tilted FM on the third AFM patch. $CrBr_3$ satisfies the assumptions for the analytical estimate of the critical angle using eq 5 better than CrI_3 because the size of the AFM patches is smaller and they are well-separated (Figure 1h). This
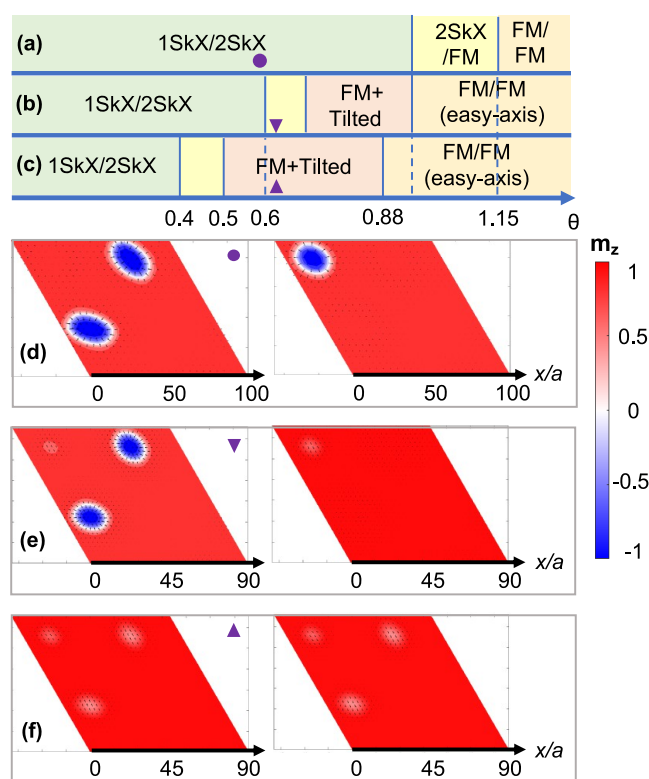
estimate gives θ_c for the skyrmionic phase transition $\sim 0.5°$, $0.7°$, and $1.4°$ for $D/J = 0.05$, 0.1 and 0.2, respectively, consistent with the 2SkX/FM to FM/FM phase boundary that takes place at $\theta_c \sim 0.5°$, $0.7°$, and $1.15°$. Given the good agreement achieved between our M_z/M_s calculations and experimental data in CrI_3, we also calculate M_z/M_s for $CrBr_3$. The overall magnetization drop in this case is much less pronounced (different scale between left and right panels in Figure 3) because the AFM patches are smaller than in CrI_3. The overall angle dependence remains similar for the different D/J values, with the magnetization dropping gradually for $D/J = 0.05$ and 0.1, while a more abrupt change is obtained for $D/J = 0.2$. At small angles, saturation is reached at $M_z/M_s \sim 0.9-0.95$. On the basis of our results, twisted bilayer $CrBr_3$ is a promising system to study because it should also display a rich phase diagram with nontrivial magnetic phases.

Finally, we discuss the phase diagram for $CrCl_3$ (panels a−c of Figure 5). Similar to CrI_3 and $CrBr_3$, a FM/FM phase is the
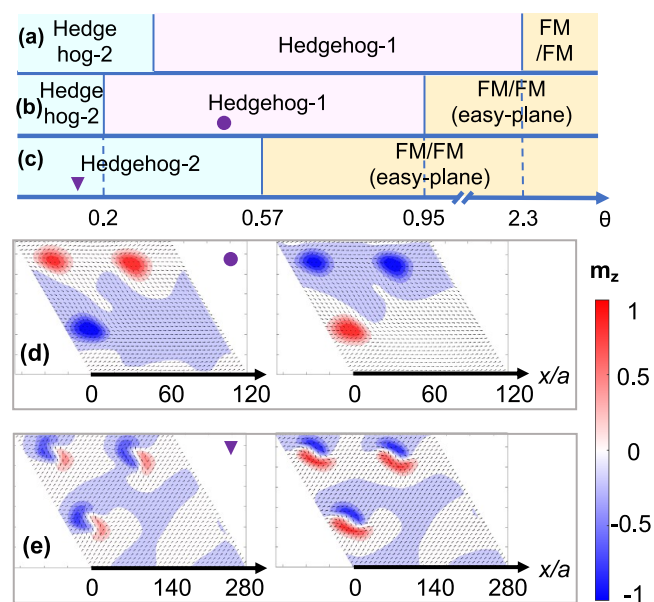

Figure 5. Phase diagram and magnetization textures of twisted bilayer $CrCl_3$. (a−c) Phase diagram of twisted bilayer $CrCl_3$ as a function of the twist angle θ for different values of the DMI. Here, panels a, b, and c correspond to $D/J = 0.2$, 0.1, and 0.05, respectively. (d) Magnetization texture of Hedgehog-1 for $D/J = 0.1$ and $\theta = 0.48°$. (e) Magnetization texture of Hedgehog-2 for $D/J = 0.05$ and $\theta = 0.2°$. The x axis in panels d and e shows the real space position within the moiré unit cell.

Figure 4. Phase diagram and magnetization textures in twisted bilayer $CrBr_3$. (a−c) Phase diagram of twisted bilayer $CrBr_3$ as a function of the twist angle θ for different values of DMI. Here, panels a, b, and c correspond to $D/J = 0.2$, 0.1, and 0.05, respectively. (d) Magnetization texture of 1SkX/2SkX for $D/J = 0.2$ and $\theta = 0.57°$. (e) Magnetization texture of 2SkX/FM for $D/J = 0.1$ and $\theta = 0.64°$. (f) Magnetization texture of the FM + tilted state for $D/J = 0.05$ and $\theta = 0.64°$. The x axis in panels d−f shows the real space position within the moiré unit cell.

ground state for large angles, with the distinction that, in this case, the magnetization is in-plane, which prevents SkX formation at small angles. Instead, two noncollinear magnetic orders arise, labeled as Hedgehog-1 and Hedgehog-2 (panels d and e of Figure 5), in which the in-plane magnetization acquires an out-of-plane component around the AFM patches that is opposite in the two layers. Hedgehog-1 resembles a meron configuration as the magnetization points up (or down) at the cores and in plane at the edges. However, unlike merons (or antimerons), the magnetization does not wind at the edges and, therefore, does not have a half-integer quantized topological charge. The Hedgehog-2 configuration has similar features, with a single AFM patch resembling a meron−antimeron pair. However, it also does not have the proper in-

plane winding of the spins and, therefore, does not have a quantized topological charge. The topological charge distribution of these two phases is presented in the Supporting Information.

In conclusion, we have shown that the interplay of the stacking-dependent interlayer exchange, twist angle, and DMI can lead to noncollinear magnetic states in bilayer chromium trihalides. In particular, we demonstrate that for small twist angles various skyrmion crystal phases can be stabilized in both CrI_3 and $CrBr_3$, whereas for large angles all three systems are ferromagnetic. While we have focused here on homobilayer chromium trihalides, our approach provides a general framework for understanding chiral magnetism in twisted 2D magnets. Interesting directions for future work include the effects of gating and external magnetic field as well as the study of heterobilayers (CrX_3/CrX_3') combining different halide ions. In this situation, the lattice mismatch will give rise to a moiré pattern even without twisting. The effects of strain[33,34] and interlayer separation[12] are also interesting paths to explore.

ASSOCIATED CONTENT

Ⓢ Supporting Information

The Supporting Information is available free of charge at https://pubs.acs.org/doi/10.1021/acs.nanolett.1c02096.

> Structural parameters, comparison of exchange–correlation functionals, magnetic shape anisotropy, continuum free energy, topological charge density of $CrCl_3$, domain wall energy, and critical angle estimation (PDF)

AUTHOR INFORMATION

Corresponding Authors

Onur Erten − *Department of Physics, Arizona State University, Tempe, Arizona 85287, United States;* ⓞ orcid.org/0000-0002-1944-239X; Email: onur.erten@asu.edu

Antia S. Botana − *Department of Physics, Arizona State University, Tempe, Arizona 85287, United States;* Email: antia.botana@asu.edu

Authors

Muhammad Akram − *Department of Physics, Arizona State University, Tempe, Arizona 85287, United States*

Harrison LaBollita − *Department of Physics, Arizona State University, Tempe, Arizona 85287, United States*

Dibyendu Dey − *Department of Physics, Arizona State University, Tempe, Arizona 85287, United States;* ⓞ orcid.org/0000-0002-2639-3266

Jesse Kapeghian − *Department of Physics, Arizona State University, Tempe, Arizona 85287, United States*

Complete contact information is available at:
https://pubs.acs.org/10.1021/acs.nanolett.1c02096

Author Contributions

†Muhammad Akram and Harrison LaBollita contributed equally to this work.

Notes

The authors declare no competing financial interest.

REFERENCES

(1) Cao, Y.; Fatemi, V.; Fang, S.; Watanabe, K.; Taniguchi, T.; Kaxiras, E.; Jarillo-Herrero, P. Unconventional superconductivity in magic-angle graphene superlattices. *Nature* **2018**, *556*, 43−50.

(2) Tong, Q.; Liu, F.; Xiao, J.; Yao, W. Skyrmions in the moiré of van der Waals 2D Magnets. *Nano Lett.* **2018**, *18*, 7194−7199.

(3) Hejazi, K.; Luo, Z.-X.; Balents, L. Noncollinear phases in moiré magnets. *Proc. Natl. Acad. Sci. U. S. A.* **2020**, *117*, 10721−10726.

(4) Hejazi, K.; Luo, Z.-X.; Balents, L. Heterobilayer moiré magnets: Moiré skyrmions and the commensurate-incommensurate transition. *arXiv.org, e-Print Arch., Condens. Matter* **2021**, arXiv:2009.00860v2 https://arxiv.org/abs/2009.00860v2.

(5) Akram, M.; Erten, O. Skyrmions in twisted van der Waals magnets. *Phys. Rev. B: Condens. Matter Mater. Phys.* **2021**, *103*, L140406.

(6) Handy, L. L.; Gregory, N. W. Structural properties of chromium(III) iodide and some chromium(III) mixed halides. *J. Am. Chem. Soc.* **1952**, *74*, 891−893.

(7) Morosin, B.; Narath, A. X-Ray diffraction and nuclear quadrupole resonance studies of chromium trichloride. *J. Chem. Phys.* **1964**, *40*, 1958−1967.

(8) McGuire, M. A.; Dixit, H.; Cooper, V. R.; Sales, B. C. Coupling of crystal structure and magnetism in the layered, ferromagnetic insulator CrI_3. *Chem. Mater.* **2015**, *27*, 612−620.

(9) Blei, M.; Lado, J. L.; Song, Q.; Dey, D.; Erten, O.; Pardo, V.; Comin, R.; Tongay, S.; Botana, A. S. Synthesis, engineering, and theory of 2D van der Waals magnets. *Appl. Phys. Rev.* **2021**, *8*, 021301.

(10) McGuire, M. Crystal and magnetic structures in layered, transition metal dihalides and trihalides. *Crystals* **2017**, *7*, 121.

(11) Sivadas, N.; Okamoto, S.; Xu, X.; Fennie, C. J.; Xiao, D. Stacking-dependent magnetism in bilayer CrI_3. *Nano Lett.* **2018**, *18*, 7658−7664.

(12) Klein, D. R.; MacNeill, D.; Song, Q.; Larson, D. T.; Fang, S.; Xu, M.; Ribeiro, R. A.; Canfield, P. C.; Kaxiras, E.; Comin, R.; Jarillo-Herrero, P. Enhancement of interlayer exchange in an ultrathin two-dimensional magnet. *Nat. Phys.* **2019**, *15*, 1255−1260.

(13) Gibertini, M. Magnetism and stability of all primitive stacking patterns in bilayer chromium trihalides. *J. Phys. D: Appl. Phys.* **2021**, *54*, 064002.

(14) Xiao, F.; Chen, K.; Tong, Q. Magnetization textures in twisted bilayer CrX_3 (X = Br, I). *Phys. Rev. Research* **2021**, *3*, 013027.

(15) Huang, B.; Clark, G.; Navarro-Moratalla, E.; Klein, D. R.; Cheng, R.; Seyler, K. L.; Zhong, D.; Schmidgall, E.; McGuire, M. A.; Cobden, D. H.; Yao, W.; Xiao, D.; Jarillo-Herrero, P.; Xu, X. Layer-dependent ferromagnetism in a van der Waals crystal down to the monolayer limit. *Nature* **2017**, *546*, 270−273.

(16) Li, T.; Jiang, S.; Sivadas, N.; Wang, Z.; Xu, Y.; Weber, D.; Goldberger, J. E.; Watanabe, K.; Taniguchi, T.; Fennie, C. J.; Fai Mak, K.; Shan, J. Pressure-controlled interlayer magnetism in atomically thin CrI_3. *Nat. Mater.* **2019**, *18*, 1303−1308.

(17) Song, T.; Fei, Z.; Yankowitz, M.; Lin, Z.; Jiang, Q.; Hwangbo, K.; Zhang, Q.; Sun, B.; Taniguchi, T.; Watanabe, K.; McGuire, M. A.; Graf, D.; Cao, T.; Chu, J.-H.; Cobden, D. H.; Dean, C. R.; Xiao, D.; Xu, X. Switching 2D magnetic states via pressure tuning of layer stacking. *Nat. Mater.* **2019**, *18*, 1298−1302.

(18) Chen, W.; Sun, Z.; Wang, Z.; Gu, L.; Xu, X.; Wu, S.; Gao, C. Direct observation of van der Waals stacking-dependent interlayer magnetism. *Science* **2019**, *366*, 983−987.

(19) Xu, Y.; Ray, A.; Shao, Y.-T.; Jiang, S.; Weber, D.; Goldberger, J. E.; Watanabe, K.; Taniguchi, T.; Muller, D. A.; Mak, K. F.; Shan, J. Emergence of a noncollinear magnetic state in twisted bilayer CrI_3.

arXiv.org, e-Print Arch., Condens. Matter **2021**, arXiv:2103.09850 https://arxiv.org/abs/2103.09850.

(20) Kresse, G.; Furthmüller, J. Efficient iterative schemes for ab initio total-energy calculations using a plane-wave basis set. *Phys. Rev. B: Condens. Matter Mater. Phys.* **1996**, *54*, 11169−11186.

(21) Blöchl, P. E. Projector augmented-wave method. *Phys. Rev. B: Condens. Matter Mater. Phys.* **1994**, *50*, 17953−17979.

(22) Perdew, J. P.; Ruzsinszky, A.; Csonka, G. I.; Vydrov, O. A.; Scuseria, G. E.; Constantin, L. A.; Zhou, X.; Burke, K. Restoring the density-gradient expansion for exchange in solids and surfaces. *Phys. Rev. Lett.* **2008**, *100*, 136406.

(23) Grimme, S.; Antony, J.; Ehrlich, S.; Krieg, H. A consistent and accurate ab initio parametrization of density functional dispersion correction (DFT-D) for the 94 elements H-Pu. *J. Chem. Phys.* **2010**, *132*, 154104.

(24) Liechtenstein, A. I.; Anisimov, V. I.; Zaanen, J. Density-functional theory and strong interactions: Orbital ordering in Mott-Hubbard insulators. *Phys. Rev. B: Condens. Matter Mater. Phys.* **1995**, *52*, R5467−R5470.

(25) Lu, X.; Fei, R.; Zhu, L.; Yang, L. Meron-like topological spin defects in monolayer $CrCl_3$. *Nat. Commun.* **2020**, *11*, 4724.

(26) Jang, S. W.; Jeong, M. Y.; Yoon, H.; Ryee, S.; Han, M. J. Microscopic understanding of magnetic interactions in bilayer CrI_3. *Phys. Rev. Materials* **2019**, *3*, 031001.

(27) Kim, H. H.; Yang, B.; Li, S.; Jiang, S.; Jin, C.; Tao, Z.; Nichols, G.; Sfigakis, F.; Zhong, S.; Li, C.; Tian, S.; Cory, D. G.; Miao, G.-X.; Shan, J.; Mak, K. F.; Lei, H.; Sun, K.; Zhao, L.; Tsen, A. W. Evolution of interlayer and intralayer magnetism in three atomically thin chromium trihalides. *Proc. Natl. Acad. Sci. U. S. A.* **2019**, *116*, 11131−11136.

(28) Soriano, D.; Cardoso, C.; Fernández-Rossier, J. Interplay between interlayer exchange and stacking in CrI_3 bilayers. *Solid State Commun.* **2019**, *299*, 113662.

(29) Soriano, D.; Katsnelson, M. I.; Fernández-Rossier, J. Magnetic two-Dimensional chromium trihalides: A theoretical perspective. *Nano Lett.* **2020**, *20*, 6225−6234.

(30) Lado, J. L.; Fernández-Rossier, J. On the origin of magnetic anisotropy in two dimensional CrI_3. *2D Mater.* **2017**, *4*, 035002.

(31) Herrera Diez, L.; Liu, Y. T.; Gilbert, D. A.; Belmeguenai, M.; Vogel, J.; Pizzini, S.; Martinez, E.; Lamperti, A.; Mohammedi, J. B.; Laborieux, A.; Roussigné, Y.; Grutter, A. J.; Arenholtz, E.; Quarterman, P.; Maranville, B.; Ono, S.; Hadri, M. S. E.; Tolley, R.; Fullerton, E. E.; Sanchez-Tejerina, L.; Stashkevich, A.; Chérif, S. M.; Kent, A. D.; Querlioz, D.; Langer, J.; Ocker, B.; Ravelosona, D. Nonvolatile Ionic Modification of the Dzyaloshinskii-Moriya Interaction. *Phys. Rev. Appl.* **2019**, *12*, 034005.

(32) Gilbert, T. L. A phenomenological theory of damping in ferromagnetic materials. *IEEE Trans. Magn.* **2004**, *40*, 3443−3449.

(33) Webster, L.; Yan, J.-A. Strain-tunable magnetic anisotropy in monolayer $CrCl_3$, $CrBr_3$, and CrI_3. *Phys. Rev. B: Condens. Matter Mater. Phys.* **2018**, *98*, 144411.

(34) León, A. M.; González, J. W.; Mejía-López, J.; de Lima, F. C.; Morell, E. S. Strain-induced phase transition in CrI_3 bilayers. *2D Mater.* **2020**, *7*, 035008.